ADVANCED FUNCTIONAL MATERIALS
www.afm-journal.de

# Enhancing the Performance of the Mesoporous $TiO_2$ Film in Printed Perovskite Photovoltaics through High-Speed Imaging and Ink Rheology Techniques

*Sarah-Jane Potts,* Rebecca Bolton, Tom Dunlop, Kathryn Lacey, Carys Worsley, Trystan Watson, and Eifion Jewell*

**Mesoscopic carbon-based perovskite solar cells (C-PSCs) have the potential to be manufactured at an industrial scale by utilizing screen-printing, a simple, affordable, and commercially mature process. As such, many recent publications have focused on enhancing performance through modifying cell architecture and perovskite chemistries. This work examines how ink rheology can be tuned to optimize cell performance through reducing the occurrence of common print defects to create higher quality m-$TiO_2$ films. Inks with different solvent dilutions and rheological profiles are assessed using high-speed imaging through the screen-printing visualization (SPV) technique, to investigate the impact of the viscosity and elasticity on ink separation mechanisms. The resultant film quality and its influence on device performances are then assessed. Ink separation lengths are minimized, and the formation of filaments ceases during printing, leading to improved $TiO_2$ film topography and homogenous infiltration of the perovskite precursor. Consequently, PCE is improved by over 10% of the original efficiency in cells and 224 $cm^2$ active area modules due to enhanced $V_{oc}$ and FF. These results not only provide key insights into tailoring ink rheology, to achieve improved print homogeneity and higher performing cells, but also aid further work on enhancing the performance of other screen-printed functional films.**

## 1. Introduction

Perovskite solar cells (PSCs) have become an increasingly viable alternative to traditional monocrystalline silicon devices, with PSCs recently achieving a power conversion efficiency (PCE) of 26% at 1 sun.[1] However, these record efficiencies are typically produced with lab-scale methods of limited commercial viability, such as spin-coating.[1–4] Printed mesoscopic carbon-based perovskite solar cells (C-PSCs) are an alternative architecture manufactured using screen-printing, a relatively simple, affordable, and commercially mature process that can produce industrial scale devices.[5–8] These multi-layer devices consist of sequentially screen-printed mesoporous films of $TiO_2$, $ZrO_2$ and carbon.[9–11] After the binder is removed, a lead halide organic precursor is infiltrated through the printed films via drop casting or inkjet printing and heated to form the perovskite light absorber.[12,13] Large-scale C-PSC modules have already been fabricated using sustainable, non-toxic solvents, such as $\gamma$-valerolactone (GVL), helping further improve the commercial viability.[14–16]

Infiltration, the extent to which perovskite fills the mesoporous stack, is intrinsically linked to device performance and perovskite crystal morphology.[17,18] Cross-sectional SEM analyses have confirmed that the uniformity of the infiltrated perovskite solution across the mesoporous layers significantly impacts device performance.[19,20] As a complex, multi-interface structure, there are many ways in which this can be influenced. For example, precursor composition, substrate and solution temperature, and graphite flake orientation can all influence infiltration.[17,18]

The thickness and roughness of the printed mesoporous layers can also have a notable impact on infiltration and resultant C-PSC performance. Li et al. found that increasing $ZrO_2$ film thickness enabled PCE improvements from 8.37% to 11.33% by preventing detrimental $TiO_2$ to carbon electron transfer.[21] Similar results were obtained by Lee et al. where increases in $ZrO_2$ thickness of up to 204 nm led to improvements in cell PCE, while further increases in film thickness led to a reduction.[22] A study by Wan et al. assessed the impact of lowering $TiO_2$ ink and altering print parameter settings, producing very thin mesoporous $TiO_2$ films of 500–550 nm thickness for C-PSCs, although this study does not relate these findings to resultant cell performances.[23]

However, changes in print surface topography and roughness, which can also heavily influence precursor infiltration or

S.-J. Potts, R. Bolton, T. Dunlop, K. Lacey, C. Worsley, T. Watson, E. Jewell
SPECIFIC
Faculty of Science and Engineering
Swansea University
Bay Campus, Crymlyn Burrows, Swansea SA1 8EN, UK
E-mail: sarah-jane.potts@swansea.ac.uk

The ORCID identification number(s) for the author(s) of this article can be found under https://doi.org/10.1002/adfm.202401959



**DOI: 10.1002/adfm.202401959**

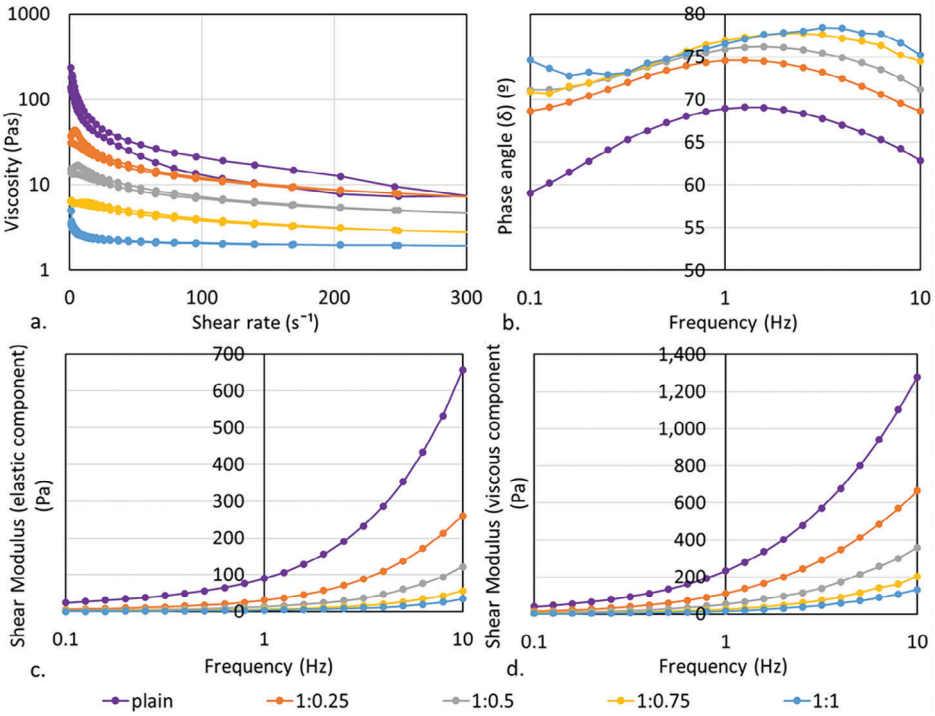


**Figure 1.** Viscosity profiles assessing changes in viscosity with a) shear rate and viscoelastic profiles assessing changes in phase angle ($\delta$); b) storage modulus (elastic component of shear modulus) ($G'$); c) and loss modulus (viscous component of shear modulus) ($G''$) with changes in frequency; d) for the different paste to dilutant ratios for the $TiO_2$ inks.

resultant cell performance due to interfacial homogeneity, are not thoroughly examined in such works. Modifying ink rheology and process parameters are known to significantly impact topography,[24–28] which has been found in some studies to have a nonlinear relationship with film thickness. Therefore, it cannot be assumed that optimal print topography relates to optimal film thickness.[29] Despite this, the impact of ink rheology or print topography on resultant cell performance has yet to be thoroughly examined.[9,15,23,30,31]

Screen-printing visualization (SPV) is an emerging technique that enables improvements in ink characteristics and process parameters by minimizing the formation of print defects such as agglomerates and mesh marking (regular features corresponding with the frequency of the mesh).[32–34] This technique utilizes high-speed imaging to visualize and quantify key ink separation stages which occur during the screen-printing process. The SPV technique has previously been used to identify optimal carbon concentrations and morphologies to improve printed film roughness, homogeneity, and conductivity. These results also demonstrated a clear correspondence between the ink separation stage lengths and the resultant topographical profile of the printed films produced.[33]

The mesoporous $TiO_2$ electron transporting layer (ETL), often produced with a commercial product such as 30 NR-D Titania Paste, is regularly reported as requiring dilution in C-PSC literature, with paste to dilutant ratios of between 1:1 and 1:6 by weight commonly used.[9,15,30,31] However, there are limited studies as to what constitutes the optimal paste to dilutant ratio for ensuring smooth, conformal layers and how this may influence precursor infiltration.

Therefore, a study was undertaken to improve the understanding of how the m-$TiO_2$ paste to dilutant ratio influences the inks rheological profile, separation mechanisms and resultant print topographical profile, in terms of film thickness and roughness in order to optimize the performance of the C-PSCs (Supporting Information). This was coupled with statistical performance analyses of completed cells, to quantify the impact of changes observed in print topography on device performance. Microscopic analyses of the cells and photoluminescence analyses of the m-$TiO_2$ film were also conducted to identify whether this change in printed film profile impacts perovskite infiltration.

## 2. Results and Discussions

### 2.1. Rheological Analyses

Rheological analyses were conducted to quantify the viscosity and viscoelasticity profiles of the different paste to dilutant ratios. These profiles influence how the ink flows through the screen and subsequently separates, determining the volume of ink deposited and its topographical surface profile. The shear rheological data is presented in **Figure 1**, as charts of viscosity against shear rate (*a*), phase angle against oscillation frequency (*b*), elastic modulus ($G'$) against oscillation frequency (*c*), and viscous modulus ($G''$) against oscillation frequency.

The viscosity profile in Figure 1a displays the change in viscosity for all dilutions under assessment, with increasing and then decreasing shear rates. All dilutions show a notable reduction in viscosity with increasing shear rate, indicating shear thinning (pseudoplastic) behavior. This would enable the ink to flow

more readily when experiencing the higher shear rates which occur during the screen-printing process. Additionally, they all exhibit minimal hysteresis, owing to a rapid recovery time in the initial viscosity. This would reduce ink spread following deposition, which is beneficial for minimizing the loss of print resolution. However, this can be problematic if there are unwanted print defects, such as mesh marking and agglomerations, which benefit from a longer hysteresis to reduce the print roughness.

The reduction in viscosity was greatest for the plain ink between 1 and 30 $s^{-1}$, although there was a continuous reduction in viscosity with shear rate up to the maximum rate of 300 $s^{-1}$. Similar viscosity profiles were obtained from the diluted inks, although these produced increasingly lower viscosities at all shear rates assessed with increasing dilutant concentration and showed less hysteresis. The difference between the viscosity at rest and the viscosity obtained at the maximum shear rate also became less significant as the ratio of dilutant increased. The reduction in resistance to flow is a result of decreasing $TiO_2$ particle concentration in the solvent-resin matrix, enabling greater ease of particle alignment and minimal hydrodynamic disturbances in the ink flow.[35,36]

As shown in Figure 1b the elevated dilutant ratio also led to increases in the phase angle ($\delta$) due to reductions in particle-polymer and particle-particle interactions, causing a greater relative reduction in the elastic modulus ($G'$) than the viscous modulus ($G''$). $G''$ was considerably larger than $G'$ by almost a factor of two in all instances as shown in Figure 1c,d respectively. This resulted in a more dominant viscous response with high phase angles of at least 69° at 1 Hz, increasing to over 75° with dilution. These low levels of elasticity would result in rapid separation of the ink from the substrate, which could minimize the formation of print defects such as mesh marking and agglomerations.

The increase in $\delta$ was most significant between the plain ink and the 1:0.25 dilutant ratio (Figure 1b), with the changes in $\delta$ becoming less notable as the ratio of solvent increased further. The 1:0.75 and 1:1 paste to dilutant ratios have the same $\delta$ value at three different points, with the 1:0.75 dilution having lower $\delta$ at the frequencies below 0.3 Hz and above 2 Hz, but higher $\delta$ than the 1:1 dilution ratio between these points.

This reducing change in $\delta$ indicates that there are less significant differences in the viscoelastic profile with greater increases in the concentration of dilutant, despite the viscosity continuing to gradually reduce. This could imply that further reductions in ink viscosity may not be required for minimizing the presence of print defects which impede the functionality of the printed film. In which case, the 1:0.75 paste to dilutant ratio could be optimal for maximizing the m-$TiO_2$ film's performance.

### 2.2. Ink Separation Mechanisms during Printing

The mechanisms by which the ink separates between the mesh and substrate during screen printing is critical to enabling the production of a coherent printed film which is defect free, smooth, and highly performing. The SPV technique was used to identify how the rheological profiles of the different $TiO_2$ paste to dilutant ratios influenced the ink separation mechanisms occurring during screen-printing. The quantified, cross-sectional areas of the screen-printing ink separation process for each of the paste to dilutant ratios are shown in **Figure 2**a, with images of the print interface on the left, and charts of the relative lengths of the ink separation stages on the right, as outlined in Figure 2b.[32] The average length of the paste flow ahead of the squeegee was also quantified in Figure 2a, but displayed no significant changes beyond standard deviation for the different paste to dilutant ratios tested, which aligns with findings from previous studies.[33,34]

The plain $TiO_2$ ink displays a high concentration of filaments forming during the final stages of ink separation, leading to significant peaks and troughs in the print surface after separation. This is indicated by the long flow to separation stage of 593 µm. The presence of these filaments have been directly linked to the formation of print defects such as mesh marking in previous studies.[33,34] The plain ink also exhibits a high adhesion to extension stage length of 1082 µm, leading to a long distance for ink separation between the mesh and substate. This prolonged interaction between the ink, mesh and substrate could also impact on the resultant printed film homogeneity.

Both ink separation lengths gradually reduce until the paste to dilutant ratio of 1:0.75. At this point, no filamentation during ink separation is observed, leading to a flow to separation stage of zero, along with the lowest adhesion to extension stage length of 840 µm. This would result in a printed film with a reduction in film roughness and the presence of print defects. The trends observed here are likely due to the greater interparticle distance of higher dilutions. This results in fewer particle-particle interactions and more liquid like behavior, producing less filamentation at the point of separation with increasing solvent concentration. Comparable results have been observed when assessing carbon pastes, which are also used in these perovskite cells.[33]

Further increases in dilutant concentration beyond the paste to dilutant ratio of 1:0.75 had no impact on filamentation, with the flow to separation stage remaining at zero for the 1:1 paste to dilutant ratio. However, this had a negative impact on the adhesion to extension stage, which increased to 906 µm. This might be a result of the 1:0.75 and 1:1 paste to dilutant ratios having similar phase angles, despite the continued reduction in viscosity for the 1:1 ratio, as described in Section 2.1 (Figure 1).

This indicates that phase angle may have a more dominant effect on ink separation mechanisms than viscosity and therefore provide a better indicator for an inks aptitude to produce a smooth, defect free, highly performing film. Whereas the viscosity continues to gradually reduce with further increases in solvent concentration in this instance (Figure 1a). Therefore, the 1:0.75 paste to dilutant ratio has the greatest potential, providing a filament free ink separation with the shorter separation lengths than lower dilutions, minimizing print defects. While also containing more $TiO_2$ particles to act as a hole barrier and ETL than the 1:1 paste to dilutant ratio.

### 2.3. Film Thickness and Topography

Ink dilution is known to impact the volume of ink deposited during printing. The resultant "wet film" thickness is informative, in that it enables a more accurate representation of the film deposited prior to solvent removal. Thermogravimetric analysis (TGA) was conducted to provide an estimate of the mass lost during drying for wet film thickness calculations.

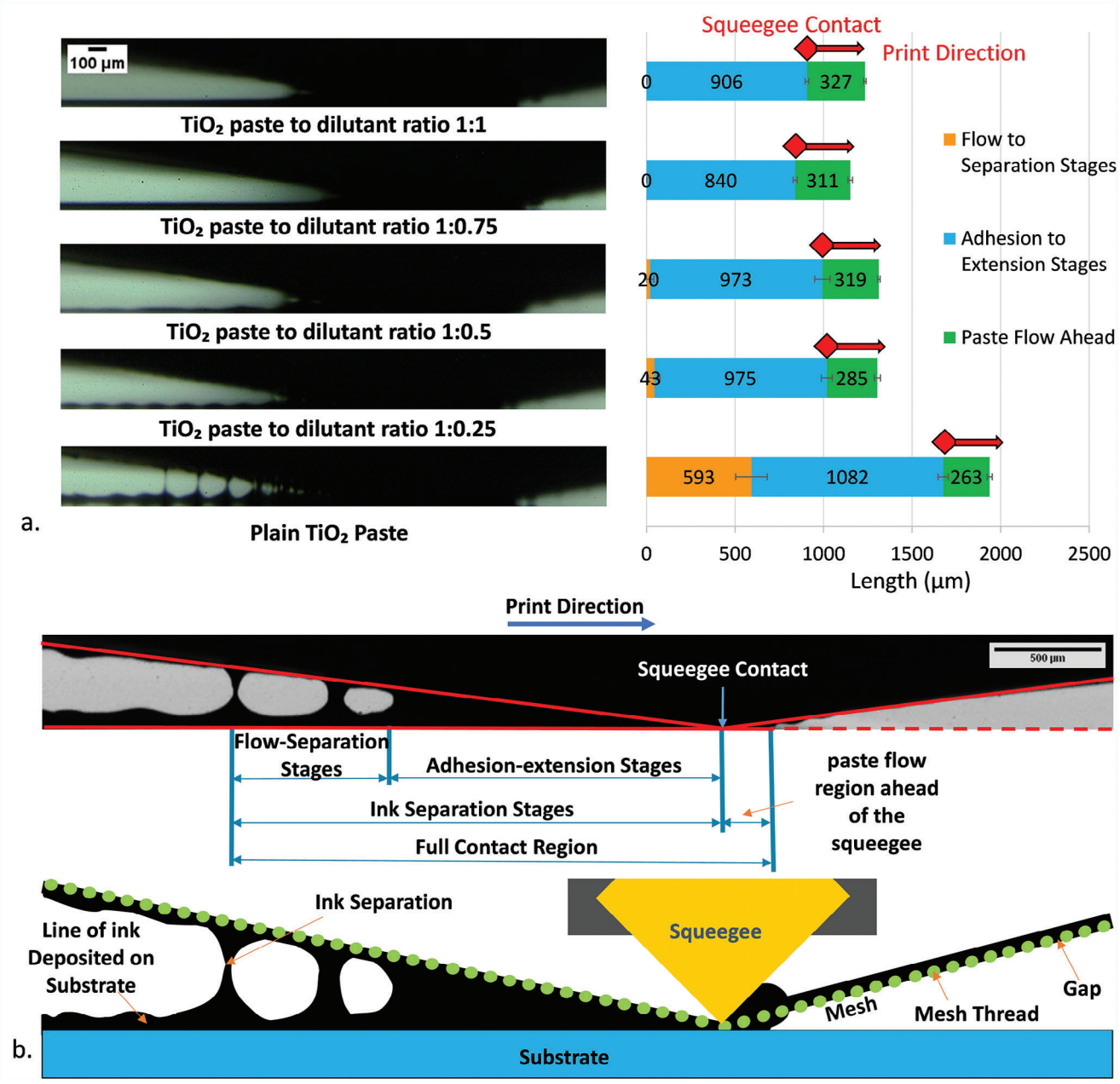


**Figure 2.** a) High-speed camera images at 5 times magnification and accompanying quantification of average print stage lengths for $TiO_2$ ink deposition of different paste to dilutant ratios (error bars represent standard deviation) with b) the labelled high-speed camera image conducted on the screen-printing visualizer (SPV), identifying the two key ink separation stages occurring during ink separation, along with the length of paste flow region ahead of the squeegee contact point (Reproduced with permission.[32] 2020, J. Coatings Technol. Res).

Thus, enabling comparisons in the amount of ink deposited prior to solvent losses from drying to be made for the different paste to dilutant ratios. The TGA graph in **Figure 3** displays the change in mass fraction measured with gradual heating to 550 °C, which is the maximum temperature attained during $TiO_2$ sintering when manufacturing C-PSCs. The mass values plateau at around 450 °C, indicating that all solvents and binder materials have been fully removed. Therefore, the titanium dioxide accounts for 20.4% of the original mass of the ink.

As the ink is heated to 550 °C during $TiO_2$ sintering, all solvents and binders will be successfully removed from the printed film, as required for C-PSCs functionality. When diluting the ink down a solvent to paste ratio of 1:1, this would result in the mass of titanium dioxide accounting for around 10% of the total ink weight.

Topography analyses were conducted with white light interferometry on the dried and cured printed films to provide a comparison between the ink separation mechanisms and print quality produced. The average ink film thickness and surface roughness

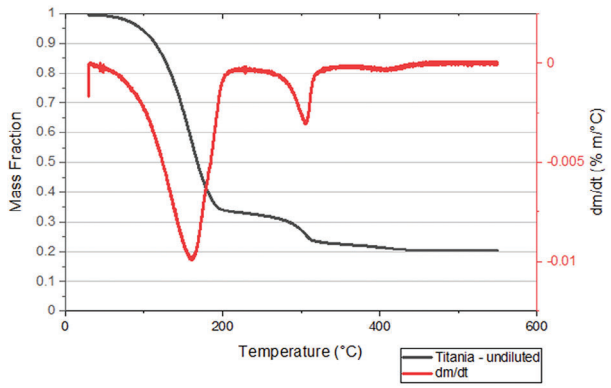


**Figure 3.** Thermogravimetric analyses of the plain (undiluted) $TiO_2$ ink up to 550 °C.

values of the printed films are shown in **Figure** 4a,b respectively, along with corresponding topography images in Figure 4c and higher magnification images of the cured films in Figure 4d. The roughness and average height values were calculated based on 1.2 mm by 0.93 mm sections conducted at 5x magnification to enable the variations in print roughness and height across the samples to be accounted for. There was a gradual reduction in the average print film thickness with increasing solvent concentrations, from 1.7 µm for the plain, undiluted ink to 0.8 µm for the 1:1 paste to dilutant ratio. The most significant reductions in average film height were between the plain ink and the 1:0.25 paste to dilutant ratio, with the values for the 1:0.5 to 1:1 paste to dilutant ratios producing film thicknesses within standard deviation of each other.

When solvent content is considered, the changes in wet film thickness underline the interaction between the process, solids content and material rheology. As with the average dry film thickness, the plain, undiluted ink still has the highest average wet film thickness, but this then suddenly drops for the 1:0.25 and 1:0.5 paste to dilutant ratios, before significantly increasing back up for the 1:0.75 paste to dilutant ratio, with a smaller increase up to the 1:1 sample. This indicates that the more dilute pastes produced a thicker wet film than those of the 1:0.25 and 1:0.5 paste to dilutant ratios, with the reduction in average height of the dry film being less than that of the increase in solvent concentration. The greater quantity of wet paste being deposited is likely due to the clean ink separation preventing excess ink being left behind on the mesh, as observed in the ink separation cross sections, shown in Figure 2a. Above a 1:0.5 paste to dilutant ratio, enhancement of transfer by viscosity reduction does not compensate for the reduction in solids and the film subsequent contraction during drying. This is supported by the high-resolution white light interferometry images (0.3 mm by 0.23 mm images conducted at 20x magnification) of the cured film profiles shown in Figure 4d. In the films produced with the plain ink to 1:0.5 paste to dilutant ratio, mesh marking can be seen in the form of characteristic spaced peaks and troughs left by the mesh on the printed film but ceases in the 1:0.75 paste to dilutant ratio film. The presence of these mesh marks on the printed film are directly related to the formation of filaments during separation, as proven in previous studies.[33,34]

The impact of increasing dilutant levels on the topography of the dried films was also assessed in terms of average surface roughness across 1.2 mm by 0.93 mm sections (Figure 4c). The average print surface roughness (Sa) reduces notably from the plain to the diluted inks. The 1:0.5 paste to dilutant ratio produces the lowest average $S_a$ value of around 206 µm, with $S_a$ increasing back up to around 294 µm with further dilution. However, the 0.3 mm by 0.23 mm images show that the 1:0.5 paste to dilutant ratio still displays some subtle mesh marks over the print surface. As $S_a$ is observing the average surface roughness, this low value may be due to a uniform distribution of peaks and troughs from particle agglomerations and pinholes respectively. When comparing the average maximum surface roughness ($S_z$) of the films, the plain ink has the highest $S_z$ value by far at around 7 µm, most likely due to the severe presence of mesh marking and other print defects. Whereas the $S_z$ of the dilutions are around 4–5 µm, with relatively little difference between the films due to the presence of particle agglomerates and mesh marks across the film areas. However, the presence of these print defects appears the least frequent in the 1:0.75 paste to dilutant ratio sample in the 0.3 mm by 0.23 mm white light interferometry images.

To provide further analyses of these print defects, scanning electron microscopy images were also conducted on the cured films, as shown in **Figure 5**. As with the higher resolution white light interferometry images, the impact of mesh marking can be observed in the plain and lower dilution level inks. This is most prominent in the plain ink analyses (Figure 5a) which demonstrated a notable ridge of agglomerated particles formed by one of the lines from the mesh marks. In the plain ink to 1:0.5 paste to dilutant ratio films (Figure 5a–c), a series of mounds and troughs from agglomerations of particles, alongside voids indicating the presence of pinholes can be seen. Similar defects are also observed in the 1:1 paste to dilutant ratio film (Figure 5e), where insufficient distributions of $TiO_2$ particles across the film have also led to regions of high and low particle concentrations, once again resulting in agglomerations and pin holes. In contrast, the 1:0.75 paste to dilutant ratio printed film was smoother and more even, without the regular presence of these print defects. Thus, providing a more uniform hole barrier and ETL than the other films.

### 2.4. Cell Performance and Infiltration Quality

C-PSCs were fabricated with the 1:0.5, 1:0.75 and 1:1 paste to dilutant ratios as their rheological properties and dry film thicknesses were within the required window for the m-$TiO_2$ film (typical film thickness of 0.4–1 µm after curing).[8,37–39] Whereas the plain ink and 1:0.25 paste to dilutant ratio produced inconsistent coverage of the m-$TiO_2$ across the printed film and were unable to create functioning cells. The statistical results for the cells are presented in **Figure 6**. Those fabricated with the 1:0.75 paste to dilutant ratio produced the highest average PCE of 13.5% ± 0.7, with a maximum forward PCE of 14.4% from the hero cell. Cells produced with 1:0.5 and 1:1 paste to dilutant ratios performed less well, with average forward PCEs of 11.5% ± 1.0 and 12.3% ± 0.3, and hero cells of 12.9% and 12.8% PCE respectively. The improved performance of the 1:0.75 paste to dilutant ratio was a consequence of elevated open-circuit voltage ($V_{oc}$) and fill

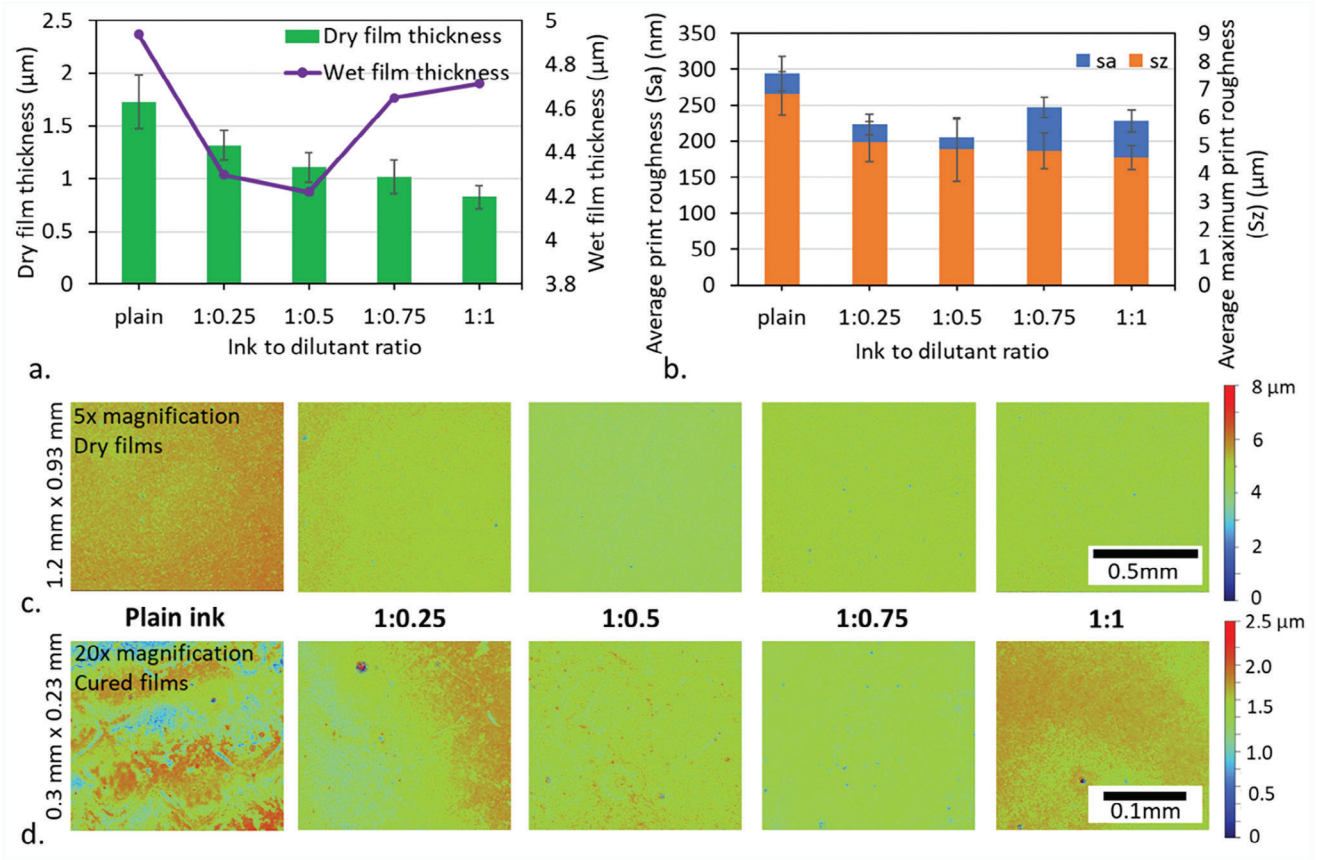


**Figure 4.** Average film thickness (wet and dry) a), average surface roughness ($S_a$) and maximum surface roughness ($S_z$) b) of the printed films (error bars for standard deviation), with corresponding white light interferometry topography images of the surface of the prints conducted for the different paste to dilutant ratios at c) 5-times magnification and d) 20-times magnification for the cured films.

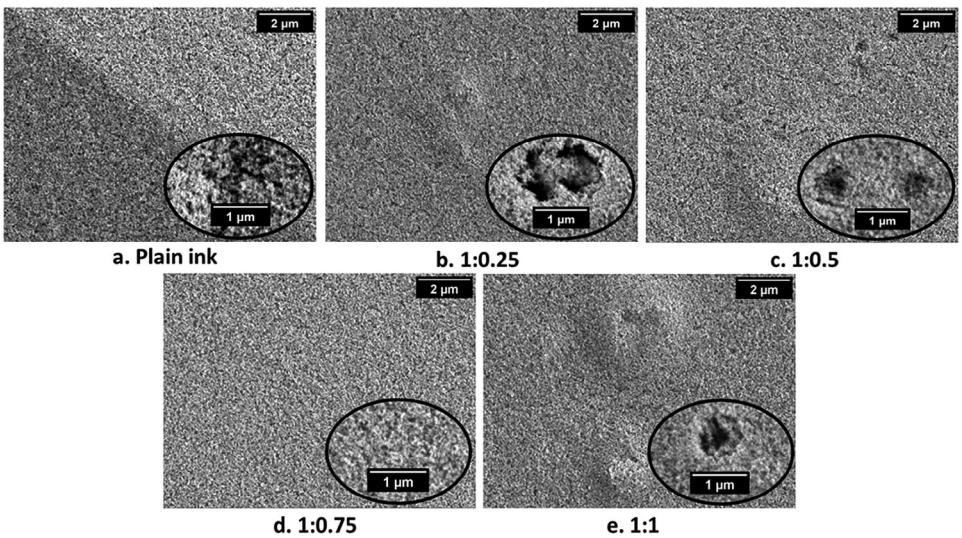


**Figure 5.** Scanning electron microscope (SEM) images showing the microstructure of the cured $TiO_2$ printed films for the different paste to dilutant ratios (a–e) at 10000-times magnification and 20000-times magnification on inset images.

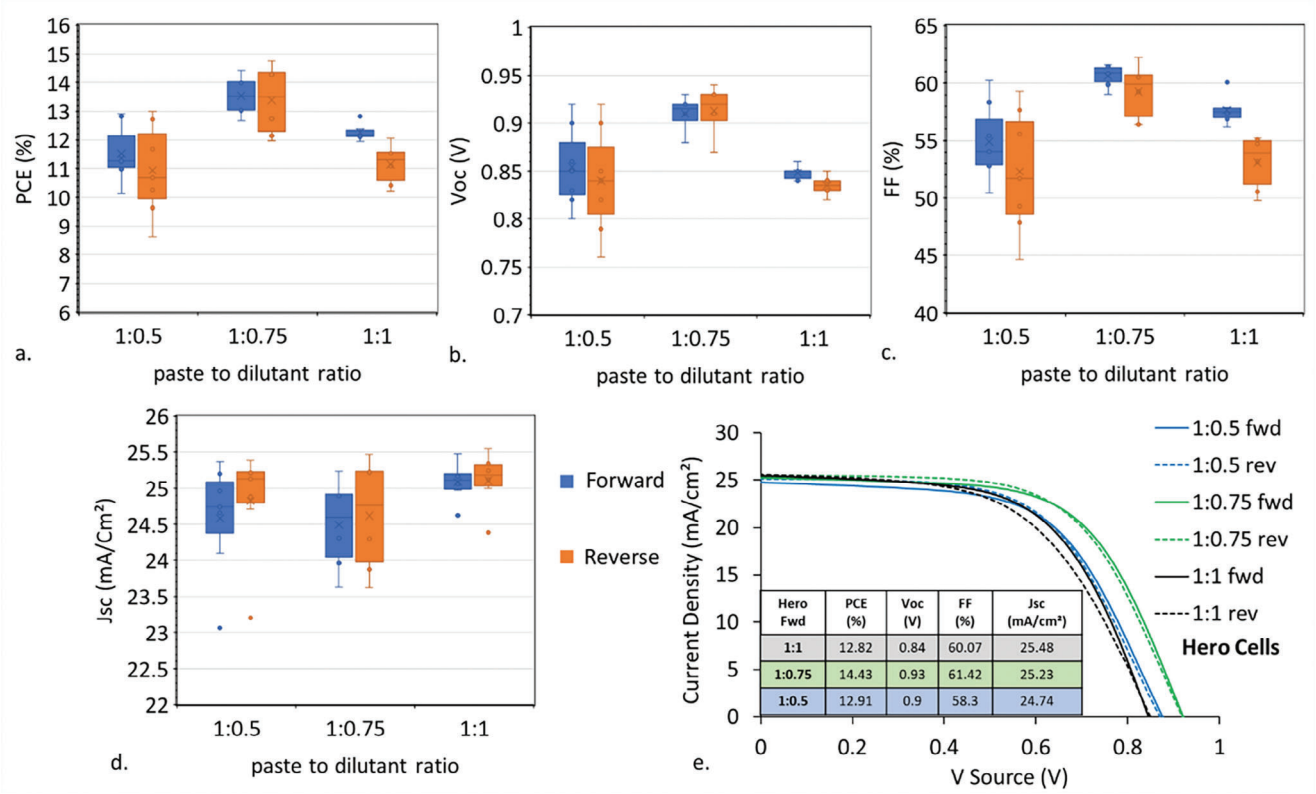


**Figure 6.** Box plot of a) *I–V* PCE, b) $V_{oc}$, c) FF, and d) $J_{sc}$ values for the devices with different paste to dilutant ratios in the mesoporous titanium dioxide layer, along with the *I–V* curves of the champion device for each paste to dilutant ratio e), under 1 sun AM1.5G illumination (based on five cells for each set).

factor (FF), although there was not a significant change in short-circuit current density ($J_{sc}$).

Infiltration inconsistencies can also result in significant performance loss on device scale-up. For a stable, high-performance module, all contributing devices must exhibit consistently high PCE across the active area. Therefore, the presence of print defects such as mesh marks, other agglomerations and pinholes across a printed film could be detrimental. As shown in **Figure 7**, a similar improvement in the performance of 224 $cm^2$ active area modules is observed when comparing the 1:0.75 paste to dilutant ratio with the commonly used paste to dilutant ratio of 1:1.[9,15,30,31] There were notable increases in the $V_{oc}$, but only a small change in the short-circuit current density $J_{sc}$ of the module, as with the cells. There were also significant reductions in hysteresis, likely a result of the improved evenness of the printed film and resultant perovskite infiltration, as found in previous studies.[15] This resulted in increases in PCE from 6.4% to 9.9% in the reverse direction and from 8.7% to 9.5% in the forward direction when changing from the commonly used paste to dilutant ratio of 1:1, to 1:0.75.

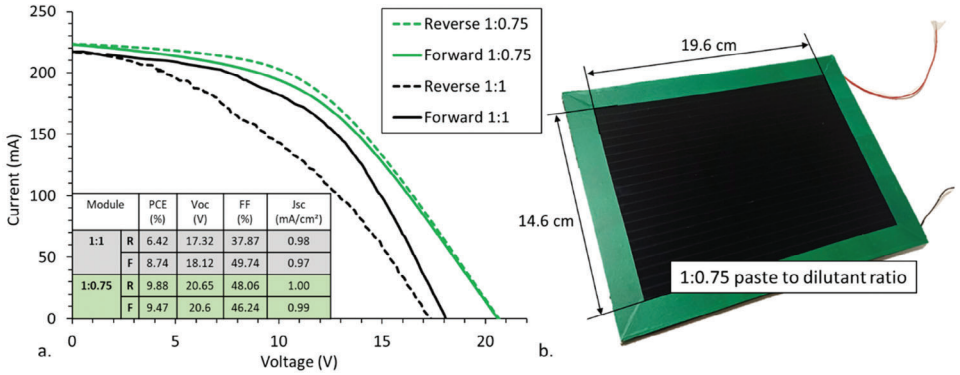


**Figure 7.** a) *I–V* curves of hero modules fabricated with 1:0.75 and 1:1 $TiO_2$ paste to dilutant ratios, with inlaid table showing measured photovoltaic parameters, conducted under 1 sun AM1.5G illumination. b) Photograph of the 1:0.75 $TiO_2$ paste to dilutant ratio module with dimensions labeled.

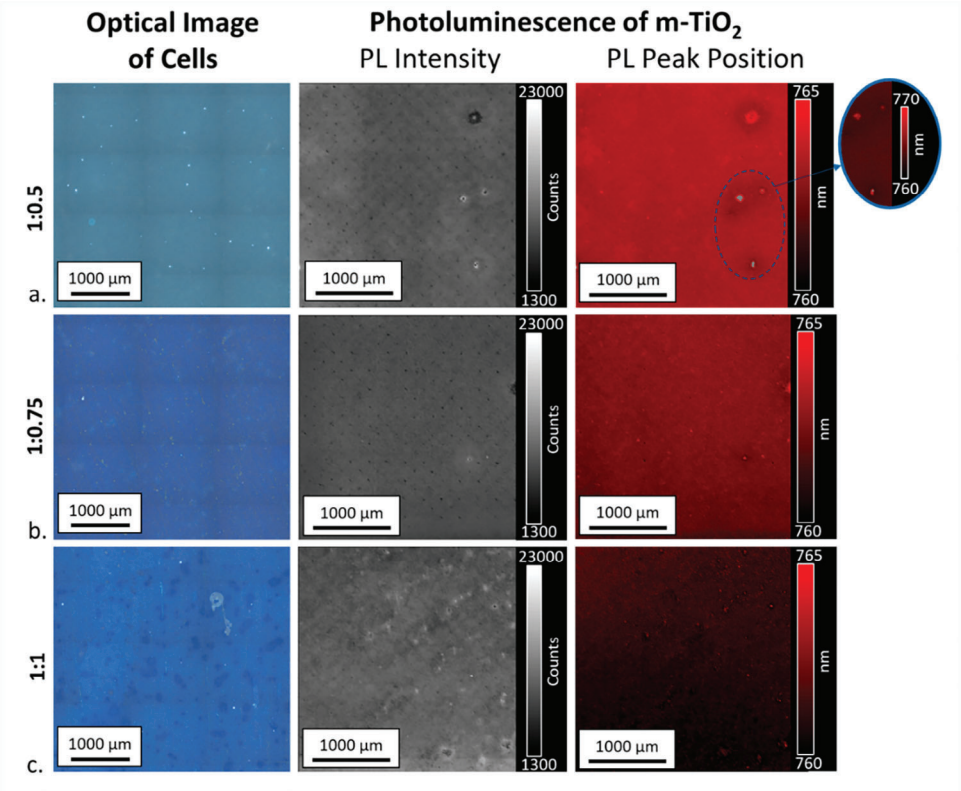


**Figure 8.** 4000 × 4000 µm optical microscopy images of resultant device infiltration imaged through the glass substrate of the cells, with 3000 × 3000 µm PL peak intensity and PL peak position maps of the infiltrated m-$TiO_2$ films (capped with carbon to enable even infiltration to occur) for a) 1:0.5, b) 1:0.75 and c) 1:1 paste to dilutant ratios.

These changes in both the cell and module performances are most likely a result of improved infiltration coherence across the film, leading to an increased $V_{oc}$ and reduction in hysteresis. This is likely due to the minimization of particle agglomerations and pinholes, enabling a more even particle distribution across the film, as observed in Figures 5d and 6. Whereas the lack of change in $J_{sc}$ may be a result of insignificant changes in the perovskite crystallinity, as all other aspects remain constant.

This improvement in infiltration coherence can be observed in the optical microscopy and photoluminescence maps, shown in **Figure 8**. These provide a macroscopic representation of device infiltration, with variations in infiltration quality across the cells and m-$TiO_2$ layer. All maps and optical images were taken from the substrate side. This optical microscopy technique has been found in previous studies to identify the impact of print related defects on the infiltration quality.[19,40] Optical microscopy images of the 1:0.5 and 1:1 paste to dilutant ratio cells shown in Figure 8a,c respectively, reveal clearly nonuniform films. Perovskite-free areas are visible as bright regions on the 1:0.5 sample, which could represent pinholes in the $TiO_2$ film due to agglomerations and mesh marking, aligning with the film microstructure shown in Figure 5.[40] Conversely, the 1:1 paste to dilutant ratio cell presented with large circular darker and lighter regions. This is likely a consequence of the excessive dilution leading to varying concentrations of $TiO_2$ (and thus perovskite) across the printed film, once again leading to print defects, including particle agglomerations and pinholes as shown in Figure 5. The 1:0.75 paste to dilutant ratio cell shown in Figure 8b also shows some lighter colored circular features, although these show a less significant contrast than the other devices, suggesting a more uniform infiltration distribution, resulting from a more coherent film.

The PL intensity maps were conducted on the plain m-$TiO_2$ film infiltrated with the perovskite solution (capped with carbon to enable even infiltration to occur) to provide a more thorough analysis of this layer. The PL intensity and peak position maps correlate well with the optical images, with circular regions of notably higher and lower PL intensity present more in the 1:0.5 and 1:1 paste to dilutant ratio samples. The PL intensity map of the 1:0.75 paste to dilutant ratio remains more uniform across the entire region, indicating a more even and coherent perovskite infiltration. It should be noted that there is the presence of small dark dots present across all three PL intensity maps, these are a feature of the mesh marks of the carbon ink. These are identifiable from their spacing of around 164 µm, the frequency of the carbon screen's mesh, rather than the spacing of the $TiO_2$ mesh which is around 77 µm.

This is also supported by the cross-sectional SEM images of infiltrated cells with EDS analyses, shown in **Figure 9**. Conformal infiltration of the perovskite precursor was observed down to the FTO layer in the 1:0.75 paste to dilutant cell in the cross-sectional analyses (Figure 9b). The m-$TiO_2$ layer was also significantly more homogeneous for this cell, whereas the 1:0.5 and 1:1 paste to dilutant ratio cells displayed less homogeneous

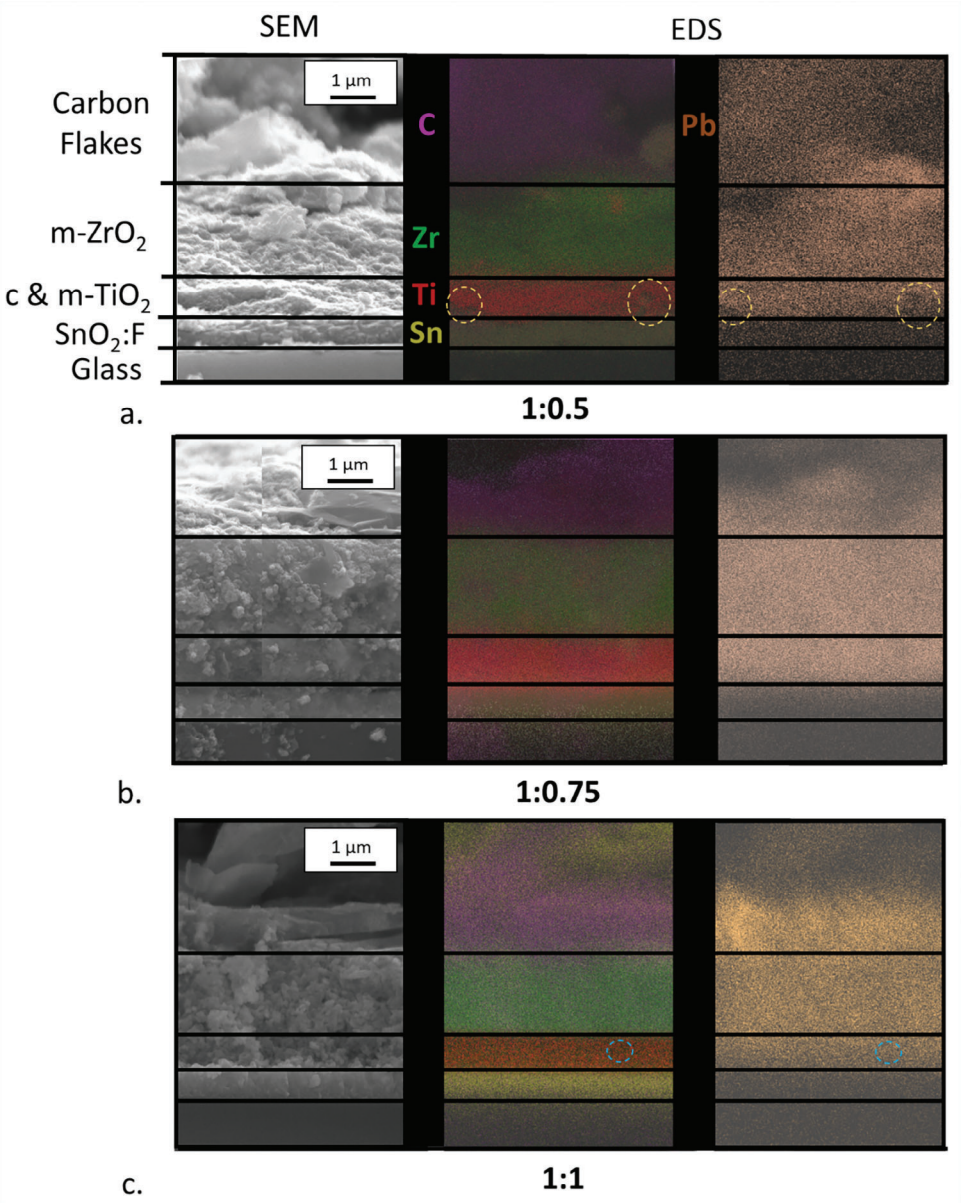


**Figure 9.** Scanning electron microscopy of the cross-sectional views of the infiltrated cells with corresponding EDS maps of the same sections for a) 1:0.5, b) 1:0.75 and c) 1:1 paste to dilutant ratios.

distributions of $TiO_2$, as highlighted by the dashed circles indicating regions of incoherent $TiO_2$ distribution. This also led to more patchy perovskite distributions, indicated by the presence of lead (Figure 9a,c). This aligns with the observed reduction in peaks and troughs forming on the surface of the printed films during ink separation for the 1:0.75 paste to dilutant ratio due to the lack of filamentation during ink separation (Figure 2a). Thus, leading to a more homogeneous distribution of particles with the minimization of mesh marking, particle agglomerations and pinholes (Figures 5 and 6), enabling a more uniform distribution of perovskite precursor across the devices.

Overall, the dilution at which the formation of filamentation ceases and separation lengths are minimized produced the highest performing and most consistently infiltrated cells and modules. This is due to the minimization of print defects such as mesh marking, particle agglomerations, and pinholes. This confirms that print topography has a significant impact on infiltration. Topography does not change linearly with film thickness, as it is dependent on the complex and non-linear rheological profiles of the inks and their interaction with the mesh and substrate. Simply diluting inks to produce thinner layers does not necessarily therefore lead to higher performing cells, and cell performance cannot be predicted or optimized by adjusting only layer thickness. Indeed, although past studies have used paste to dilutant ratios of 1:1 or higher to obtain optimum layer thickness, these results show that paste to dilutant ratios beyond 1:0.75 move beyond the optimum point for this particular paste and solvent combination.[9,15,23,30,31]

Studies on printed layer optimization should therefore conduct rheological and printing studies alongside dilution and other forms of ink modifications, to concurrently optimize both thickness and topography. This approach could be used to optimize print quality and performance of the other inks used in C-PSC fabrication, as well as those used in other screen-printed electronics such as electrochemical sensors, batteries, and solid oxide fuel cells.

## 3. Conclusion

This work demonstrates the significant impact of $TiO_2$ film topography on C-PSC infiltration and performance. Combined rheological analysis and SPV is used to identify the paste to dilutant ratio at which filamentation is prevented, improving wet film topography through minimizing mesh marking and other print defects. This in turn enables more homogeneous perovskite precursor infiltration and significantly enhanced device PCE, $V_{oc}$ and FF at the optimal ratio of 1: 0.75 for both cells and modules.

These results indicate that there is a point where further reductions in viscosity do not lead to further improvements in print quality and demonstrate that true layer optimization cannot be achieved through thickness modification alone. A concurrent approach considering both thickness and topology should therefore be applied when optimizing screen printed layers for thin film devices such as C-PSCs.

## 4. Experimental Section

*Characterization of Ink Rheology*: The study used a commercial $TiO_2$ ink by Greatcell Solar Materials (30 NR-D Titania Paste) as supplied and diluted 1:0.25, 1:0.5, 1:0.75 and 1:1 by weight with terpineol. Rheological evaluation was carried out using a combination of shear and viscoelastic measurements. Shear viscosity measurements were carried out on a Malvern Bohlin rotational rheometer (Gemini Bohlin Nano, Malvern Instruments, Malvern Panalytical Ltd, Malvern, UK) with a 2° 20 mm stainless steel cone and a parallel plate held at 25 °C. Ink viscosity was measured as the shear rate was gradually increased to 100 $s^{-1}$ and then reduced back to 1 $s^{-1}$. Viscoelastic measurements were carried out on a Malvern Kinexus Pro Rheometer (Malvern Instruments, Malvern Panalytical Ltd., Malvern, UK) with a 1° 50 mm stainless steel cone and a parallel plate. Amplitude (strain) sweep measurements were conducted to establish the linear viscoelastic range at 0.1, 1, and 10 Hz. Then using a stress within the established linear viscoelastic region, a frequency sweep from 0.1:10 Hz was conducted.

*Screen-Printing Visualization*: The mesh-substrate ink separation occurring during screen-printing was captured on a high-speed camera (Photron FastCam Mini High-Speed Camera) at a frame rate of 125 frames per second, with 8 × magnification, and a 10000-lux lamp used for backlighting. The printing was conducted on a custom- made screen-printing apparatus, the screen-printing Visualizer (SPV) (described in detail previously).[32–34] A polyester mesh at 22.5° with 130 threads per cm, 34 µm thread diameter and 9-micron emulsion was used to print the image. A 65–70 Shore A hardness diamond squeegee was used, along with a snap distance (distance between screen and substrate) of 1.825 mm and squeegee travel speed of 300 cm $min^{-1}$ (50 mm $s^{-1}$). The substrate was PET (polyethylene terephthalate—Melinex 339, DuPont Teijin Films (175 µm thickness) opaque white). The print image consisted of a continuous 75 µm wide line in the direction of squeegee travel.

The ink separation was quantified with two key regions, the adhesion to extension region (where the ink remains in continuous contact with the mesh and substrate), and the flow to separation region (where the main body of ink splits off into filaments that eventually separate) (Figure 1). A total of 45 sets of measurements were taken for each ink (15 sets of measurements conducted for each of the three prints, across evenly spaced intervals in the region assessed with high-speed imaging) from which the average and standard deviation in each of the print stages for each dilution was calculated.

*Thermogravimetric Analyses (TGA)*: TGA was used to establish the evaporative characteristics of the plain, undiluted ink to provide an estimate of the mass lost during drying to enable the wet film thickness values to be estimated. This was carried out by a Perkin Elmer Pyris 1 (Perkin Elmer Inc., Waltham, MA, United States) analysis with a temperature ramp to 550 °C over a period of 2 h (4.6 °C $min^{-1}$) in a nitrogen atmosphere to allow evaporation of the solvent content and decomposition of the binder.

*Characterization of Print Topography*: White light interferometry (NT9300, Veeco Instruments, Inc., Plainview, NY, USA) was used to measure a full 3D surface profile of printed squares of $TiO_2$. 5× magnification was used for printed film thickness and roughness analyses, giving a measurement area of 1.2 mm by 0.93 mm (at a resolution of 736 pixels × 480 pixels with sampling at 1.67 µm intervals). The dry ink film thickness was evaluated by measuring over the edge of the solid print, calculated as the average thickness of the substrate subtracted from the average thickness of the ink. The wet film thickness was also calculated based on the TGA analysis of the undiluted ink, used to identify the relative mass of solvents, binders, and $TiO_2$ in the ink. As the solvents were evaporated during drying, the dry film thickness was estimated as a solvent free solid film containing the remaining binder and $TiO_2$ from the ink. Therefore, the volume percentage of the solvent lost during drying was used to estimate the wet film thicknesses for the different ink dilutions. Analyses were also conducted in the center of the print for the average surface roughness (Sa) and average maximum surface roughness ($S_z$) values. A total of eight measurements were conducted for each dilution for both surface roughness and film thickness, from which the average and standard deviation, in film thickness and surface roughness were calculated. Additionally, 20× magnification was used to provide a more detailed analysis of the cured film, giving a measurement area of 0.3 mm by 0.23 mm.

*Manufacturing of Photovoltaic Cells*: To fabricate the cells, FTO substrates (FTO glass TEC-7 2.2 mm, XOP Glass) were patterned with a Rofin Nb:$YVO_4$ laser (532 nm) at a speed of 150 mm $s^{-1}$. These were then cleaned with approximately 2% Hellmanex solution in deionized water, washed with deionized water and rinsed with acetone and IPA, then dried with N2. To deposit the compact $TiO_2$ layer, the substrates were then heated to 300 °C on a hot plate, and a solution of titanium diisopropoxide bis (acetylacetonate) (TAA, 75% in IPA, Sigma-Aldrich) with anhydrous 2-propanol (IPA, 99.5%, Sigma Aldrich) was deposited by spray pyrolysis. All layers of the triple mesoporous stack were deposited via screen printing on an ATMA AT-25PA flatbed screen printer. Each printed sample was dried in a Thieme hot dryer at 100 °C for a residence time of 20 min, then cured in a HENGLI Belt Furnace.

The $TiO_2$ layers were diluted 1:0.5, 1:0.75 and 1:1 by weight with terpineol were printed with a polyester mesh at 45° with 130 threads per cm, 34 µm thread diameter and 9-µm emulsion over mesh (EOM). A 70–75 Shore A hardness double bevel blade squeegee of 130 mm length was used, along with a snap distance (distance between screen and substrate) of 3.3 mm and squeegee travel speed of 210 mm $s^{-1}$. These were then sintered at 550 °C for 30 min after a slow ramp. The $ZrO_2$ ink (Zr-Nanoxide ZT/SP, Solaronix) was printed with the same mesh, squeegee, and print speed as the $TiO_2$ ink, but with a 4.3 mm snap distance. These were then sintered at 400 °C for 30 min after a slow ramp. The carbon ink (GEM C2150317D3 carbon paste (Gwent Electronics Materials (GEM)), diluted with 5 wt% 1-methoxy-2-propanol (Sigma)) was printed with a polyester mesh at 45° with 61 threads per cm, 64 µm thread diameter and 12 µm emulsion over mesh (EOM). A 65–70 Shore A hardness blade squeegee at 30° to the mesh was used, along with a snap distance (distance between screen and substrate) of 4.3 mm, with the same print speed as before. As with the $ZrO_2$ inks, these were then sintered at 400 °C for 30 min after a slow ramp.

All layers were cooled to room temperature in ambient conditions (30–50% RH, 18–21 °C), before drop casting of 20 ml room temperature

perovskite precursor (containing $PbI_2$ (99%, TCI), MAI ($CH_3NH_3I$, anhydrous, Greatcell Solar), 5-ammonium valeric acid iodide (5-AVAI, Greatcell Solar), g-valerolactone (GVL, Sigma Aldrich) and anhydrous MeOH (Sigma Aldrich)) onto the stack. Devices were left for 20 min in ambient conditions after drop casting precursor to ensure adequate infiltration, before annealing on a hot plate for 1.5 h at 45 °C. Contacts were applied with an ultrasonic solder at 180 °C.

*Manufacturing of Photovoltaic Modules*: The interconnects between the cells were patterned using a scribing method.[41] The P1 scribes in the FTO layer were created via a Nd:YVO4 laser. The substrates were then cleaned as per the cell fabrication method. The FTO coated 226 mm × 176 mm glass superstrate was heated to 300 °C on a hot plate and the compact $TiO_2$ blocking layer was deposited by spray pyrolysis. The mesoporous layers were once again deposited with an ATMA AT-25PA flatbed screen printer. The P2 and P3 scribes to create the interconnects in the other layers were conducted on a Workbee CNC instrument with a steel blade under 0.54 N/mm pressure, to mechanically create the patterns. The scribe widths measured 50 nm, 0.60 mm, and 0.20 mm for P1, P2 and P3, respectively, resulting in an active area of 224 $cm^2$ across 22 cells with a geometric fill factor of around 80%. The perovskite precursor was deposited via a LOCTITE 400D deposition robot at a speed of 12 m $s^{-1}$ with a 12-gauge syringe tip at 1 bar of pressure, then cured in a Thieme conveyor dryer at 45 °C for 1.5 h. Contacts were applied manually via ultrasonic soldering at 180 °C, robotic wires were subsequently soldered to the contacts. Modules were stored in a blacked out, airtight box in ambient conditions once soldered.

*Testing of Photovoltaic Cells*: The cells were masked to 0.16 $cm^2$ and placed under a fan for testing. A Keithley 2400-C source meter and class AAA solar simulator (G2V Sunbrick solar simulator) at 1 sun was used for *J–V* measurements (calibrated against a silicon reference cell, Newport Oriel 91150 V). Devices were scanned at a rate of 100 mV $s^{-1}$ from −0.2–1.1 V and vice-versa after a light soaking period of 180 s.

*Testing of Photovoltaic Modules*: A Keithley 2400-C 5A source meter and class AAA solar simulator (G2V Sunbrick solar simulator) at 1 sun was used for *J–V* measurements (calibrated against a silicon reference cell, Newport Oriel 91150 V). The devices were scanned at a rate of 70 mV $s^{-1}$ between −0.1 and 21 V in forward and reverse directions over the full device area, after a light soaking period of 180 s. For stabilized current measurements, devices were held at the maximum power point (as determined by the preceding IV scan) for a period of 200 s to account for slow device response times.

*Optical Microscopy of Cells*: Optical microscopy was used to assess the quality of infiltration over a 4000 × 4000 µm region. This was done with a Zeiss Axio Observer Z1M using darkfield imaging to improve contrast between the infiltrated and infiltrated areas. Zeiss control software was used to provide a full cell stitched image which was then opened in Zeiss ZEN Blue and an apertured 4 × 4 mm area was selected for analysis. This was done to ensure matching with the PV testing parameters. Active area was determined using a machine learning automated image segmentation which has been trained on a large number of carbon cells using the ZEN Intellesis framework to ensure high match accuracy.

*Scanning Electron Microscopy*: The microstructure of the prints was assessed using a JEOL JSL 7800F FEG scanning electron microscope (SEM). Top-down images of the $TiO_2$ films were conducted on samples that were sputter coated in 5 nm of Pt to enhance conductivity, in secondary electron scanning mode with an electron energy of 10 kV, a working distance of 10 mm, at magnifications of 10000× and 20000× . Cross sectional images were also acquired in secondary electron scanning mode with an electron energy of 15 kV, a working distance of 10 mm and magnification of 15000× . The chemical analyses of the cross sections were performed using an Oxford Instruments Ultim energy-dispersive X-ray spectroscopy (EDS) detector with an AZTEC software (Ver 5.0) analysis package (Oxford Instruments Plc, Abingdon, UK), at a 10 mm working distance with the samples angled towards the detector to improve the signal. Samples were prepared by standard fracture methods, mounted onto a conductive holder, and coated with 5 nm Pt to provide conductivity for the glass substrate.

*Photoluminescence Mapping*: Photoluminescence mapping measurements were carried out using a Renishaw InVia confocal Raman microscope by measuring the samples through the glass substrates on an X–Y scanning stage (100 nm minimum step size). Maps were produced with individual spectra at each region producing a 3000×3000 µm map for each sample. All measurements were conducted with a 5× objective lens. A 532 nm laser excitation source was used (spot size ≈ 1 µm) at 0.05 µW laser power.

## Supporting Information

Supporting Information is available from the Wiley Online Library or from the author.

## Acknowledgements

The authors acknowledge funding from the Engineering and Physical Research Council (EPSRC) (SPECIFIC IKC Phase 2, Grant reference: EP/N020863/1). Microscopy facilities were provided by the Swansea University AIM Facility; funded in part by the EPSRC (EP/M028267/ 1), the European Regional Development Fund through the Welsh Government (80708) and the Ser Solar project via Welsh Government. The authors also thank the Welsh Centre for Printing and Coating for access to the shear rheology equipment. The manuscript was written through contributions of all authors. All authors have given approval to the final version of the manuscript.

## Conflict of Interest

The authors declare no conflict of interest.

## Data Availability Statement

The data that support the findings of this study are available from the corresponding author upon reasonable request.

## Keywords

high-speed imaging, perovskite, photovoltaics, printed electronics, rheology, screen-printing, surface characterization, $TiO_2$

Received: January 31, 2024
Revised: March 26, 2024
Published online:

[1] F. Ma, Y. Zhao, Z. Qu, J. You, *Acc. Mater. Res.* **2023**, *4*, 716.
[2] Z. Skafi, J. Xu, V. Mottaghitalab, L. Mivehi, B. Taheri, F. Jafarzadeh, S. K. Podapangi, D. Altamura, M. R. Guascito, L. Barba, C. Giannini, A. Rizzo, F. De Rossi, H. Javanbakht Lomeri, L. Sorbello, F. Matteocci, F. Brunetti, T. M. Brown, *Sol. RRL* **2023**, *7*, 2300324.
[3] R. Lin, Y. Wang, Q. Lu, B. Tang, J. Li, H. Gao, Y. Gao, H. Li, C. Ding, J. Wen, P. Wu, C. Liu, S. Zhao, K. Xiao, Z. Liu, C. Ma, Y. Deng, L. Li, F. Fan, H. Tan, *Nature* **2023**, *620*, 994.
[4] A. Mishra, Z. Ahmad, *J. Mater. Sci.: Mater. Electron.* **2019**, *30*, 20320.
[5] J. Kang, H. Kim, K. S. Kim, S. K. Lee, S. Bae, J. H. Ahn, Y. J. Kim, J. B. Choi, B. H. Hong, *Nano Lett.* **2011**, *11*, 5154.
[6] A. Morrin, A. J. Killard, M. R. Smyth, *Anal. Lett.* **2003**, *36*, 2021.
[7] B. Philip, E. Jewell, P. Greenwood, C. Weirman, *J. Manuf. Process.* **2016**, *22*, 185.

[8] F. De Rossi, J. A. Baker, D. Beynon, K. E. A. Hooper, S. M. P. Meroni, D. Williams, Z. Wei, A. Yasin, C. Charbonneau, E. H. Jewell, T. M. Watson, *Adv. Mater. Technol.* **2018**, *3*, 1800156.
[9] S. M. P. Meroni, C. Worsley, D. Raptis, T. M. Watson, *Energies* **2021**, *14*, 386.
[10] J. Jestine, R. E. Johnston, C. P. Pearce, P. Davies, T. Watson, S. Meroni, C. Worsley, R. Dimitrios, T. Dunlop, R. Mitchell, T. Volkenandt, B. Tordoff, S. Kelly, R. White, M. N. Rad, *Microsc. Microanal.* **2022**, *28*, 204.
[11] D. Pourjafari, N. G. García-Peña, W. Y. Padrón-Hernández, D. Peralta-Domínguez, A. M. Castro-Chong, M. Nabil, R. C. Avilés-Betanzos, G. Oskam, *Materials* **2023**, *16*, 3917.
[12] J. Baker, K. Hooper, S. Meroni, A. Pockett, J. McGettrick, Z. Wei, R. Escalante, G. Oskam, M. Carnie, T. Watson, *J. Mater. Chem. A* **2017**, *5*, 18643.
[13] A. J. Huckaba, Y. Lee, R. Xia, S. Paek, V. C. Bassetto, E. Oveisi, A. Lesch, S. Kinge, P. J. Dyson, H. Girault, M. K. Nazeeruddin, *Energy Technol.* **2019**, *7*, 317.
[14] C. Worsley, D. Raptis, S. Meroni, A. Doolin, R. Garcia-Rodriguez, M. Davies, T. Watson, *Energy Technol.* **2021**, *9*, 2100312.
[15] C. Worsley, D. Raptis, S. M. P. Meroni, R. Patidar, A. Pockett, T. Dunlop, S. J. Potts, R. Bolton, C. M. E. Charbonneau, M. Carnie, E. Jewell, T. Watson, *Mater. Adv.* **2021**, *3*, 1125.
[16] Y. Miao, M. Ren, Y. Chen, H. Wang, H. Chen, X. Liu, T. Wang, Y. Zhao, *Nat. Sustainability* **2023**, *62*, e202312726.
[17] T. Liu, L. Liu, M. Hu, Y. Yang, L. Zhang, A. Mei, H. Han, *J. Power Sources* **2015**, *293*, 533.
[18] K. P. Goetz, A. D. Taylor, Y. J. Hofstetter, Y. Vaynzof, *ACS Appl. Mater. Interfaces* **2021**, *13*, 1.
[19] H. Lakhiani, T. Dunlop, F. De Rossi, S. Dimitrov, R. Kerremans, C. Charbonneau, T. Watson, J. Barbé, W. C. Tsoi, *Adv. Funct. Mater.* **2019**, *29*, 1900885.
[20] T. Dunlop, O. Kesteven, F. De Rossi, P. Davies, T. Watson, C. Charbonneau, *Materials* **2021**, *14*, 5852.
[21] Y. Li, L. Zhao, S. Wei, M. Xiao, B. Dong, L. Wan, S. Wang, *Appl. Surf. Sci.* **2018**, *439*, 506.
[22] H. Lee, K. Kim, O. Song, *J. Korean Inst. Met. Mater.* **2020**, *58*, 59.
[23] Z. Wan, M. Xu, Z. Fu, D. Li, A. Mei, Y. Hu, Y. Rong, H. Han, *Front. Optoelectron.* **2019**, *12*, 344.
[24] J. Hoornstra, A. W. Weeber, H. H. C. de Moor, W. C. Sinke, in *14th European Photovoltaic Solar Energy Conf. and Exhibition*, ECN, Barcelona, Spain **1997**, p. 4.
[25] B. Philip, E. Jewell, D. Worsley, *J. Coat. Technol. Res.* **2016**, *13*, 911.
[26] J. Pan, G. L. Tonkay, A. Quintero, W. P. Ave, *J. Electron. Manuf.* **1999**, *9*, 203.
[27] T. A. Molamphy, M. I. Stephenson, E. A. Murphy, *Solder. Surf. Mt. Technol.* **1992**, *11*, 4.
[28] S. H. Mannan, N. N. Ekere, I. Ismail, E. K. Lo, *IEEE Trans. Compon., Packag., Manuf. Technol., Part A* **1994**, *17*, 470.
[29] C. Phillips, A. Al-Ahmadi, S.-J. Potts, T. Claypole, D. Deganello, *J. Mater. Sci.* **2017**, *52*, 9520.
[30] D. Raptis, C. A. Worsley, S. M. P. Meroni, A. Pockett, M. Carnie, T. Watson, *Solar* **2022**, *2*, 293.
[31] E. Parvazian, A. Abdollah-zadeh, H. R. Akbari, N. Taghavinia, *Sol. Energy Mater. Sol. Cells* **2019**, *191*, 148.
[32] S.-J. Potts, C. Phillips, E. Jewell, B. Clifford, Y. C. Lau, T. Claypole, *J. Coat. Technol. Res.* **2020**, *17*, 447.
[33] S.-J. Potts, C. Phillips, T. Claypole, E. Jewell, *Coatings* **2020**, *10*, 1008.
[34] S.-J. Potts, T. Korochkina, A. Holder, E. Jewell, C. Phillips, T. Claypole, *J. Mater. Sci.* **2022**, *57*, 2650.
[35] H. A. Barnes, *A Handbook of Elementary Rheology*, Vol. *6*, The University of Wales, Institute of Non-Newtonian Fluid Mechanics, Aberystwyth **2000**.
[36] D. J. Jeffrey, A. Acrivos, *AIChE J.* **1976**, *22*, 417.
[37] G. Grancini, C. Roldán-Carmona, I. Zimmermann, E. Mosconi, X. Lee, D. Martineau, S. Narbey, F. Oswald, F. De Angelis, M. Graetzel, M. K. Nazeeruddin, *Nat. Commun.* **2017**, *8*, 15684.
[38] Y. Hu, S. Si, A. Mei, Y. Rong, H. Liu, X. Li, H. Han, *Sol. RRL* **2017**, *1*, 2.
[39] V. Kapoor, A. Bashir, L. J. Haur, A. Bruno, S. Shukla, A. Priyadarshi, N. Mathews, S. Mhaisalkar, *Energy Technol.* **2017**, *5*, 1880.
[40] C. A. Worsley, T. O. Dunlop, S. Potts, R. Garcia-rodriguez, R. S. Bolton, M. L. Davies, E. Jewell, T. M. Watson, *ACS Appl. Energy Mater.* **2024**, *7*, 1938.
[41] S. M. P. Meroni, K. E. A. Hooper, T. Dunlop, J. A. Baker, D. Worsley, C. Charbonneau, T. M. Watson, *Energies* **2020**, *13*, 1589.